Description and Validation of the `Boulder` code

Alessandro Morbidelli

Observatoire de la Côte d'Azur

Boulevard de l'Observatoire

B.P. 4229, 06304 Nice Cedex 4, France

William F. Bottke

Southwest Research Institute

1050 Walnut St, Suite 300

Boulder, CO 80302 USA

David Nesvorný

Southwest Research Institute

1050 Walnut St, Suite 300

Boulder, CO 80302 USA

Harold F. Levison

Southwest Research Institute

1050 Walnut St, Suite 300

Boulder, CO 80302 USA

Received _____; accepted _____

1. Introduction

The `Boulder` code simulates the accretion and collisional fragmentation of a population of planetesimals using a statistical, particle-in-the box approach. The planetesimals are distributed over a range of semi major axes, which can be subdivided into multiple concentric annuli. In each annulus, the planetesimal population is represented by a mass distribution. The appropriate mass range is divided in logarithmic bins. The mean ratio δm between the mean masses in adjacent bins is a free parameter of the code: in the runs presented here it has been set equal to 1.4. The definition of the mass bins (both bin center and bin width), however, evolves dynamically and adapts to the evolution of the population (moving bin algorithm). The ratio between the mean masses of adjacent bins can become as small as $\sqrt{\delta m}$ or stretch up to $(\delta m)^{3/2}$. When the mass ratio evolves outside of this range, bins are joined (if too close) or new bins are created (if the original bins are too far apart). See sect. 1.5 below for details. For each mass bin, we record the total number of objects, their total mass and mean eccentricity and inclination. All these quantities evolve in time according to algorithms accounting for accretion, collisional grinding and mutual dynamical interactions, described below.

We list here briefly the sequence of operations executed by the code at each time-step. Each operation is then detailed in a separate sub-section.

i For each pair of annuli and mass bins, the mutual intrinsic collision probability (Wetherill, 1967) and the relative impact velocity are computed. Of two interacting populations, the one with the smaller individual mass is considered to be the population of 'projectiles', whereas the other one is the population of 'targets'. If two populations have the same individual mass, each is considered both as 'projectiles' and 'targets' and the intrinsic collision probability is divided by 2. This step also identifies so-called 'isolated bodies' within each annulus. See sect. 1.1 for their definition. The

intrinsic collision probability between pairs of isolated bodies is set equal to zero.

ii The intrinsic collision probability is multiplied by the square of the sum of the radii of projectile and target, by the gravitational focusing factor, by the total numbers of projectiles and targets and by the duration of the time-step, in order to obtain the total number of collisions in the considered time interval. The number of collisions is rounded to an integer number. **This is done taking its fractional part f and calling a random number generation routine: if the result of the call is smaller than f, the number is rounded to the first higher integer; if the result is larger than f, the fractional part is dropped.**

iii For each collision, on the basis of state-of-the-art SPH simulations, we compute the mass of the largest remnant and the mass of the largest fragment, relative to the sum of the masses of projectile and target, as well as the exponent of the power-law fragment size distribution. The fragment size distribution is assumed to be continuous, from the size of the largest fragment down to the smallest recorded mass bin. The exponent of the cumulative power-law fragment size distribution is assumed to be equal to -2.5 for fragments smaller than some threshold size that is computed according to the constraint of mass conservation. In this algorithm both accretion and fragmentation are treated simultaneously.

iv Given the quantities computed at step *iii*, the largest remnant and the fragments produced by the collision are distributed among the available mass bins. The total mass and number of objects in each bin is updated at every collision. The mean eccentricities and inclinations of the objects issued from a collision are assumed to be equal to those of the target.

v After all collisions have been enacted, the eccentricities and inclinations in each mass bin are evolved according to stirring-damping equations, detailed in sec. 1.4.

vi Finally, the mass bins are re-defined. The new mass at the center of each bin is recomputed by dividing the total mass by the number of objects in the bin population (moving bin algorithm). New bins are introduced if adjacent bins separate too far apart, or old bins are joined if they are too close. It is well known that if the size distribution of the particles is truncated at some minimum mass, the collisional grinding process produces spurious waves in the particles size distribution (Marzari et al., 1995). Thus, denoting by m the minimum mass tracked self-consistently in the algorithm, the code computes a size distribution for masses smaller than m by extrapolation of the size distribution measured in the range m–$10^3 \times m$.

Steps *i*–*vi* are detailed below and validation tests are discussed as needed.

The `Boulder` code has an adaptive time-step. Step i computes the appropriate time interval so that the individual collision probability of any target does not exceed a threshold value, say 10%. Step *iv* computes the time interval so that none of the populations in each mass bin decreases more than a threshold value, say 80%; in particular no population can become negative. Step v computes the time interval so that the eccentricities and inclinations in each mass bin do not change by more than some given quantity, say 10%. If any of these three time intervals is smaller than the current time-step, the results are discarded, and the calculation is repeated with a time-step equal to the smallest of the computed time intervals. Otherwise, the step is considered successful and the next iteration is done with a step size equal to the smallest of the three computed time intervals, multiplied by a safety margin (say 70%). In this way, the time-step is kept small when the system is evolving fast, and is stretched when the system has reached a quasi-steady state situation (see sect. 1.4.8 for tests against a more sophisticated integration scheme).

1.1. Step *i*: Collision probability calculation.

We follow the classical particle-in-the box approach for the collision probability calculation (see Wetherill and Stewart, 1993, denoted WS93 hereafter). If particles i (projectiles) and j (targets) belong to the same annulus[1] the intrinsic collision probability is defined as

$$P_{\rm int}(i,j) = \frac{\alpha V_{\rm rel}(i,j)}{4Ha(\delta a + 2ae(i))} \ , \tag{1}$$

(see WS93), where $V_{\rm rel}(i,j)$ is the average collision velocity between targets and projectiles, α is a coefficient ranging from 0.57 to 0.855 depending on $V_{\rm rel}$ (WS93), H is the symmetrical mutual scale height (see eq. (4) below), a and δa are the semi major axis and width of the annulus and $e(i)$ is the mean eccentricity of the projectiles. With respect to formula (A1) in WS93, eq. (1) is generalized for a non-zero eccentricity of the projectiles, which is assumed to be not smaller than that of the targets. Denoting by V_K the Keplerian circular velocity, by I the particles' inclination and by

$$h = \sqrt{\frac{5}{8}e^2V_K^2} \ , \quad v = \sqrt{\frac{1}{2}(\sin I)^2V_K^2} \ , \tag{2}$$

the mean horizontal and vertical velocities of a particle (Kenyon and Luu, 1998), the average collision velocity between particles i and j is:

$$V_{\rm rel}(i,j) = \sqrt{h^2(i) + h^2(j) + v^2(i) + v^2(j)} \ . \tag{3}$$

The symmetrical mutual scale height is defined as:

$$H = \frac{\sqrt{2}}{\Omega}\sqrt{v^2(i) + v^2(j)}, \tag{4}$$

---

[1]All quantities in the code are two-dimensional vectors, one index referring to the annulus and the other to the mass bin. In this text, for simplicity, we use only one index. Thus particles i and j, if $i \neq j$ may either be in two different annuli, or be in two different mass bins, or both.

(formula A2 in WS93), where Ω is the Keplerian angular velocity. The coefficient α represents the difference between the collision frequency of bodies in Keplerian orbits and that based on particle-in-the-box approach, and is given in Greenzweig and Lissauer (1992) (also reported in appendix A of WS93).

When projectiles and targets do not belong to the same annulus, we compute the fraction f of the targets that visit the volume spanned by the projectiles, accounting for the eccentricities of both targets and projectiles, and we multiply eq. (1) by f. In eq. (4) the angular velocity Ω is computed in correspondence of the mean value of the semi major axes of the annuli of particles i and j.

Finally, we set equal to zero the mutual intrinsic collision probability of 'isolated bodies' belonging to the same annulus. The idea is that the isolated bodies are those which have enough room in the annulus to park themselves onto orbits with a mutual separation of a few Hill radii from aphelion to perihelion. Consequently isolated bodies do not approach each other and avoid mutual collisions. This behavior is seen in many numerical simulations (see for instance Kokubo and Ida, 1995, 1996, 1998). Thus, following WS93 (see section II.B.1 in that work), we identify 'isolated bodies' as follows. We sort the mass bins, and index them from 1 to n from the smallest to the largest mass. We denote $l_{\rm iso}$ the minimal index l such that:

$$\sum_{i=l}^{n} N(i) R_g(i) < \delta a \ , \tag{5}$$

where $N(i)$ is the total number of bodies in mass bin i, $R_g(i) = c_H R_{\rm Hill}(i) + 2ae(i)$, the quantity $R_{\rm Hill}$ is the mutual Hill radius of the bodies in the mass bin, namely:

$$R_{\rm Hill}(i) = a \left(\frac{2M(i)}{3M_\odot} \right)^{1/3} \tag{6}$$

and c_H is a parameter of the code, that we set equal to $2\sqrt{3}$, following WS93. The 'isolated bodies' are those that belong to the bins $l_{\rm iso}, \ldots, n$. Isolated bodies accrete (only) non-isolated bodies. As they grow, R_g grows as well, so that the condition (5) becomes

more restrictive as time passes. Thus, the least massive of the isolated bodies eventually become non-isolated. When this happens, they can be accreted by their former companions of the 'isolated' group.

Notice that, if a body is massive enough, condition (5) might not be satisfied (the width of the annulus may be too narrow compared to $c_H R_{\rm Hill}$). To correct for this, we also consider 'isolated body' the most massive body in the annulus, provided that (a) it is alone in its mass bin and (b) its Hill radius, multiplied by c_H, exceeds the width of the annulus where it resides. This will be important when evaluating the stirring effects of this body on the smaller planetesimals (see sect. 1.4.4).

Numerical simulations show that isolated bodies in dynamically cold disks open gaps in the planetesimal distribution and their accretion stalls. Thus, if j is an isolated body and the projectiles i have $e(i) < (M(j)/3M_\odot)^{1/3}$, we set $P_{\rm int}(i,j) = 0$.

1.2. Step *ii*: Gravitational focusing.

The total number of collisions between projectiles i and targets j in a time-step δt is

$$N_c(i,j) = P_{\rm int}(i,j) N(i) N(j) F_g(i,j) (R(i) + R(j))^2 \delta t \ , \tag{7}$$

where $P_{\rm int}(i,j)$ is given in eq. (1), $N(i)$ and $N(j)$ are the numbers of particles i and j respectively of physical radii $R(i)$ and $R(j)$ and $F_g(i,j)$ is the so-called *gravitational focusing factor*. It accounts for the fact that objects have a gravitational field, and thus can deflect the trajectories of the neighbors, thus enhancing their own geometrical cross-section.

We use the expression of the gravitational focusing factor given by Greenzweig and Lissauer (1990, 1992):

$$F_g(i,j) = E \left(1 + b \frac{V_{\rm esc}^2(i,j)}{V_{\rm rel}^2(i,j)} \right) \ , \tag{8}$$

where $V_{\rm esc}(i,j) = \sqrt{2G[M(i)+M(j)]/[R(i)+R(j)]}$ is the mutual escape velocity of bodies i and j (M is their respective mass and G is the gravitational constant), while b and E are coefficients depending on velocities and masses.

More specifically, b accounts for the fact that the eccentricities and inclinations for which $V_{\rm rel}$ is computed are only mean values. In reality there is a distribution of values of eccentricities and inclinations (typically a Rayleigh distribution), each with its own focusing factor. The mean focusing factor is *not* the focusing factor computed for the mean eccentricity and inclination (Greenzweig and Lissauer, 1992). Following WS93, we adopt $b = 2.7$ for $V_{\rm rel} > 2V_{\rm Hill}$, $b = 1$ for $V_{\rm rel} < V_{\rm Hill}$ and a linear interpolation between these two extremes for $V_{\rm Hill} < V_{\rm rel} < 2V_{\rm Hill}$. The Hill velocity $V_{\rm Hill}$ is defined as

$$V_{\rm Hill} = V_K R_{\rm Hill}/a \tag{9}$$

where $R_{\rm Hill}$ is the mutual Hill radius of particles i and j. Again, if particles i and j belong to two different interacting annuli we adopt for a and V_K the mean of the values of the respective annuli.

The coefficient E is given in the appendix B of Greenzweig and Lissauer (1990). It accounts for deviations of F_g from the classical 'two-body' gravitational focusing at low $V_{\rm rel}$, due to (a) limited thickness of the particle disk with respect $R_{\rm Hill}$ and (b) shepherding effects in the three-body problem. Figure 1 gives an illustration of both effects. It shows (solid curve) the value of F_g for a target whose physical radius is $4 \times 10^{-3} R_{\rm Hill}$ as a function of the dispersion velocity of the field projectiles, here represented by the quantity $I_{\rm Hill} = I/R_{\rm Hill}$ under the assumption that $e = 2I$. The classical two-body gravitational focusing (i.e. eq. (8) for $E \equiv 1$; line of slope -2) is shown with a dashed line, whereas a reference slope of -1 is plotted with a dash-dotted line.

As one sees, F_g follows the classical two-body gravitational focusing formula down to $I_{\rm Hill} \sim 1$. Below this value F_g follows for a while the slope -1; this is because the disk is

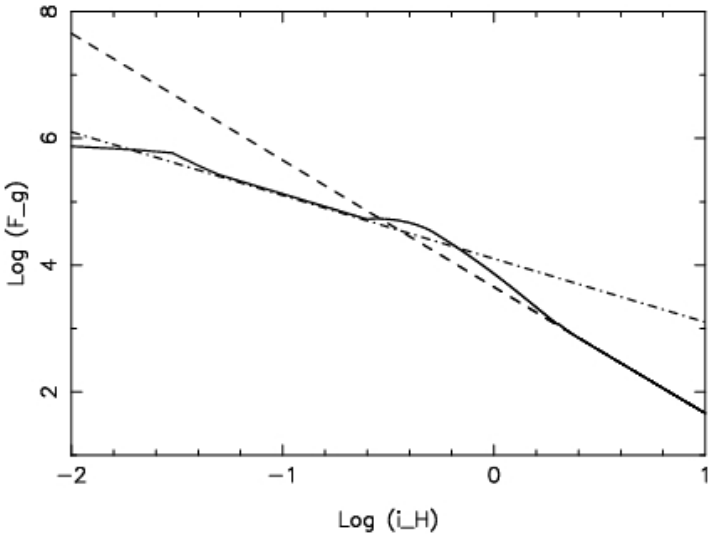

Fig. 1— The solid curve shows the value of the gravitational focusing factor as a function of the dispersion velocity of the projectiles, according to Greenzweig and Lissauer (1990). For reference, the dashed and dash-dotted lines have slope equal to -2 and -1 respectively.

thinner than the gravitational radius of the target, so that it behaves as a two dimensional system, with $F_g \propto V_{\rm esc}/V_{\rm rel}$, instead of its square. Finally, for small enough velocity (low value of $I_{\rm Hill}$), F_g becomes essentially constant (see Greenberg et al., 1991, for a discussion). This is due to shepherding effects: the extremely low velocity orbits are not more likely to hit the target, but rather avoid it following a horseshoe-like trajectory in the target corotating frame. Notice the curious 'bumps' that F_g exhibits when it branches from one asymptotic solution to another. We stress that in a disk with $I_{\rm Hill} \lesssim 0.1$ (e.g. in a disk whose ddispersion velocity is kept low relative to the Hill velocity of the largest bodies by strong gas-drag or collisional damping), runaway accretion does not occur because the F_g factor for the largest bodies is proportional $(V_{\rm esc}/V_{\rm rel})^p$, with $p \leq 1$, and ${\rm d}M/{\rm d}t \propto M^{2/3} F_g \propto M^{(2+p)/3}$.

1.3. Steps *iii*-*iv*: Collisional accretion & fragmentation.

The calculations described above tell us which fraction of the population experiences a collision during a time-step, and with which relative velocity. The outcome of the collision then depends on the mass of the projectile and the strength of the target. Fortunately we now have a good insight of the collisional outcome from SPH numerical experiments.

Following Benz and Asphaug (1999), we define Q_D^* as the specific impact energy (energy per unit target mass) required to disperse into space 50% of the target mass. The quantity Q_D^* is a function of the target radius. Several Q_D^* functions are given in the literature for different types of material. Here we use the function reported in Benz and Asphaug (1999) for basalt at impact velocity of 5km/s.

The kinetic energy of the projectile per unit mass of the target is denoted by Q. From the SPH experiments, Benz and Asphaug (1999) report that the mass of the largest remnant after a collision can be fitted as a function of Q/Q_D^* as:

$$M_{LR} = \left[-\frac{1}{2} \left(\frac{Q}{Q_D^*} - 1 \right) + \frac{1}{2} \right] M_T \tag{10}$$

for $Q < Q_D^*$ and

$$M_{LR} = \left[-0.35 \left(\frac{Q}{Q_D^*} - 1 \right) + \frac{1}{2} \right] M_T \tag{11}$$

for $Q > Q_D^*$, where M_T is the target mass. Whenever $M_{\rm LR}$ in eq. (11) turns out to be negative we assume that the target is fully pulverized and all its mass is lost below the minimal mass threshold that our code can track.

In the `Boulder` code, in order to account for fragmentation and accretion at the same time, following Stern (1996), in eq. (10) and eq. (11) we substitute M_T with $M(i) + M(j)$, i.e. the sum of the masses of projectile and target. For consistency, we also compute Q_D^* using an effective radius $r_{eff} = [(M(i) + M(j))/(4/3\pi\rho)]^{1/3}$, where ρ is the bulk density of the planetesimals. Thus, for Q much smaller than Q_D^*, the mass of the largest remnant M_{LR}

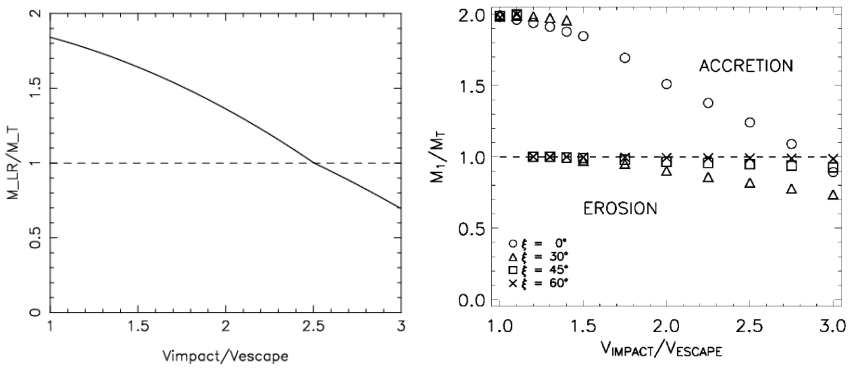

Fig. 2— Left panel: The mass resulting from the collision of two Mars-mass bodies, normalized to a Mars-mass, as a function of the impact speed relative to the mutual escape velocity. The horizontal dashed line separates the accretional from erosive regime. Right panel: reproduction of Fig. 1 of Agnor and Asphaug (2004), showing the same according to SPH simulations, at various impact angles.

can be bigger than $M(j)$, which results in effective accretion. As Q increases relative to Q_D^* the accretion becomes progressively less effective and eventually it is smoothly turned into a collisional erosion. This recipe for treating accretion and erosion simultaneously is very close to that recommended by Stewart and Leinhardt (2009).

The outcome of collisions between two Mars-mass objects at various relative velocities and impact angles was computed with SPH techniques in Agnor and Asphaug (2004). The left panel of Fig. 2 shows the result of our algorithm. It compares satisfactorily with the SPH results for an impact angle of 0° (see the right panel of the figure). We notice however that the results in Agnor and Asphaug (2004) show that accretion becomes ineffective for impact angles larger than 30°–45°. This effect, however, has not yet been tested for a variety of masses and mass ratios, so that we do not include it in our algorithm for the moment. One should keep in mind, therefore, that our code might overestimate accretion, although it is not clear the magnitude of this effect, given that most of the accretion of massive bodies is due to collisions with small bodies, and not to collisions among massive

bodies themselves (which appear in general as isolated bodies in our code, so that their mutual collisions are prevented). To our knowledge, none of the statistical accretion codes existing in the literature accounts for the -still poorly quantified- impact angle effect.

Concerning the size distribution of the fragments ejected from the collision, we calibrated our algorithm using the SPH results in Durda et al. (2007). This work conducted a large number of simulations of collisions of projectiles of various masses and velocities upon 100 km targets. Except for highly catastrophic collisions, the results typically show that the fragments have a continuous, steep power-law size distribution starting from a size -that we call 'size of the largest fragment'- that is well separated from the size of the largest remnant, defined above. We have measured the mass of the largest fragment and the slope of the power-law size distribution in each of the experiments in Durda et al. (2007), and we have tabulated them as a function of the ratio Q/Q^*_D that characterized each experiment. We found that the following laws provide reasonable empirical fits to the experimental data (see Fig. 3):

$$M_{LF} = 8 \times 10^{-3} \left[\frac{Q}{Q^*_D} \exp^{-\left(\frac{Q}{4Q^*_D}\right)^2} \right] (M(i) + M(j)) \tag{12}$$

for the mass of the largest fragment and

$$q = -10 + 7 \left(\frac{Q}{Q^*_D} \right)^{0.4} \exp^{-\frac{Q}{7Q^*_D}} \tag{13}$$

for the slope of the cumulative power-law size distribution of the fragments.

Of course, size distributions with slopes as steep as given by eq. (13) would contain an infinite mass. To avoid this problem, we assume that the fragment size distribution has a cumulative slope $q = -2.5$ (Dohnanyi, 1969) below a turn-over radius r_t. We compute r_t so that the mass integral of this two-slope power-law, from sizes ranging from 0 to the size of the largest fragment is equal to the total ejected mass (defined as $M(i) + M(j) - M_{LR}$). The fragments generated according to the resulting size distribution are then distributed into the mass bins of our code.

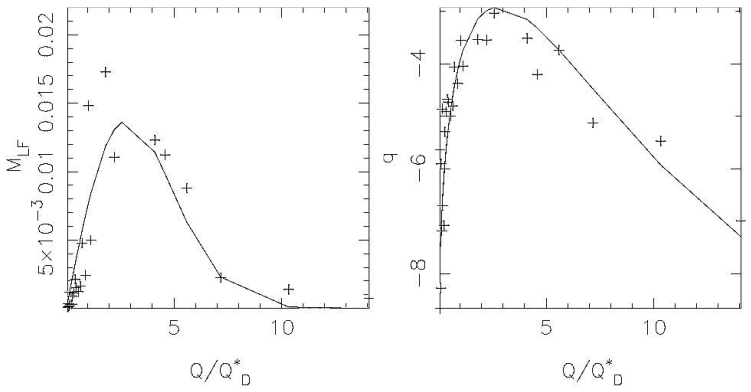

Fig. 3— Left: The mass of the largest fragment as a function of Q/Q_D^*. Right: the exponent of the power-law distribution of the fragments. Crosses denote the results of the SPH simulations of Durda et al. (2007). The curve shows the empirical fit that we adopt in the `Boulder` code.

In a collisional grinding regime, the collisional evolution of a population is ultimately governed by the size distribution of the smallest objects. Unfortunately, a statistical code can deal only with a finite number of mass bins, which imposes to truncate the population distribution at some small size. This truncation can generate spurious waves in the resulting size distribution of the overall population, even at large sizes (Marzari et al., 1995). To avoid this problem, given the mass m of the smallest object that our code tracks (an input parameter), we consider a tail of objects down to an individual mass $\mu < m$, with μ defined as the mass of the smallest object that can remove an object of mass m from its own mass bin. The value of μ changes during the simulation, as the relative velocities of the particles evolve. The evolution of the objects of masses between μ and m is not calculated self-consistently (otherwise the problem of truncation would present itself again at μ), but instead these objects are assumed to have a size distribution that extrapolates that produced by the code for masses larger than m. More details on this are given when describing step *vi*, below.

We have tested the collisional part of our code by comparing its results with those of

the collisional evolution code CoDDEM of Bottke et al. (2005, 2005b). The comparison experiment has been set up as follows. We have considered a size distribution of objects, spanning from 3m to 200 km in size, with a power-law cumulative size distribution characterized initially by exponent $q = -4$. The bulk density of the planetesimals is $1\mathrm{g/cm}^3$. The planetesimals evolve in an annulus centered at 2.5 AU, with a width of 0.5 AU. The total mass is 1.46×10^{28}g. The intrinsic collision probability and impact velocity among the objects are set constant and equal to 4.87×10^{-18} $\mathrm{km}^{-2}\mathrm{y}^{-1}$ and 8.7 km/s, respectively. This experiment is not intended to mimic any realistic condition in the asteroid belt, but just to set an extreme case for an intense collisional grinding and compare the performance of the two codes.

For a quantitative comparison we have to take into account that CoDDEM uses a series of approximations with respect to what we described above. In CoDDEM, all collisions with $Q > Q_D^*$ leave a largest remnant that has 50% of the mass of the target (independent of Q/Q_D^*). Cratering events ($Q < Q_D^*$) are ignored. Moreover a unique fragment size distribution is considered (Bottke et al., 2005), first shallow, then steep, then shallow again, starting from the size of the largest remnant, downwards (so, according to our definition above, the largest fragment coincides with the largest remnant).

We have matched the results of CoDDEM using equivalent simplifications (Fig. 4a). The match is essentially the same even if eq. (11) is adopted and for a variety of values of Q, provided that the mass of the largest fragment is 'close' (i.e. within 50%) of the mass of the largest remnant. We understand this because barely catastrophic events are the most frequent ones and because the equilibrium size distribution does not depend on the slope of the fragment size distribution (Dohnanyi, 1969).

However, if cratering events are considered (i.e. eq. (10) is followed for $Q < Q_D^*$) the size distribution that we obtain deviates from that of CoDDEM below a few kilometers

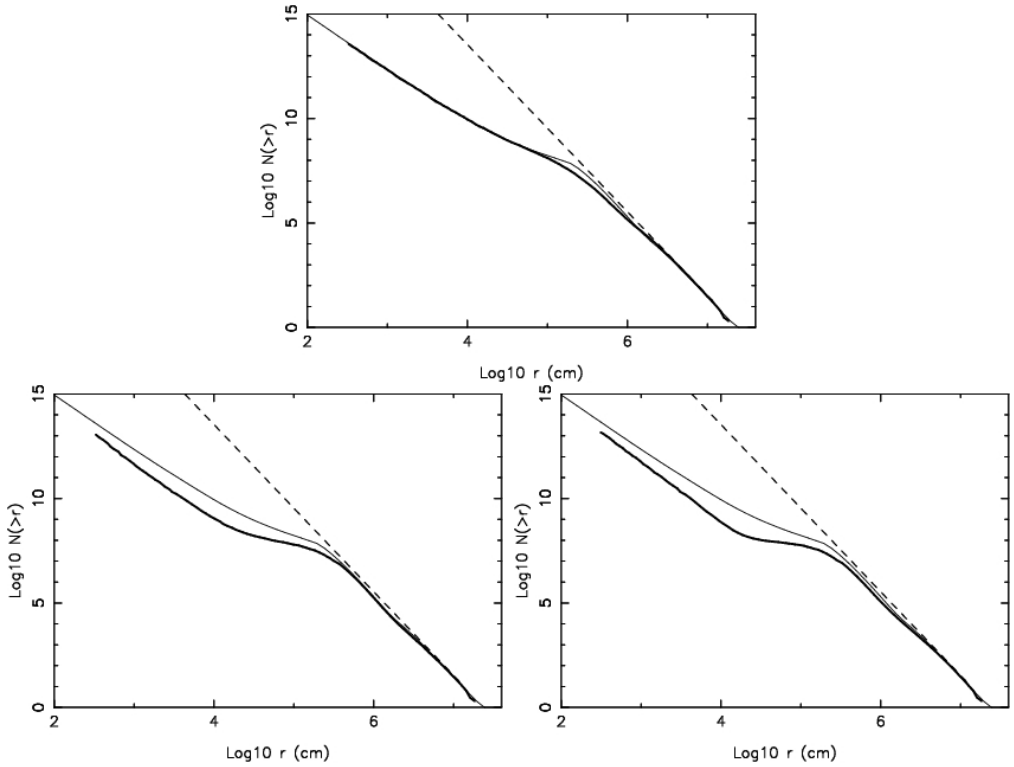

Fig. 4— The dashed line shows the initial size distribution considered in the fragmentation simulation. The solid curves show the size distribution after 6 My of evolution, according to CoDDEM (thin line, the same in all three panels) and to our code (bold line). (a) Top: simulation done neglecting cratering events and assuming that $M_{LF} = 0.5M_{LR}$ and $M_{LR} = 0.5M(j)$ when $Q > Q^*_D$. (b) Bottom left: simulation done accounting for cratering events, that is assuming that $M_{LR} = 0.5M(j)$ for $Q > Q^*_D$ and that M_{LR} is given by eq. (10) for $Q < Q^*_D$; in both cases we assume $M_{LF} = 0.5(M(i) + M(j) - M_{LR})$. (c) Bottom right: simulation done using our nominal algorithm (all the formulae described in the text).

(Fig. 4b). The wave is more pronounced and there is a deficit of objects in the range 10m – 1km. This is because, although cratering events excavate less mass than catastrophic events, they are more numerous, so their overall effect is important.

Finally, if we introduce an important gap between the size of the largest remnant and

that of the largest fragment (i.e. adopt eq. (12) and use the full set of equations described above), we get an even more pronounced wave and a stronger deficit of $\sim$ 100m objects (Fig. 4c). The reason for this is that objects in the range 100m–1km are the weakest according to the Q_D^* prescription adopted. If the gap between the largest remnant and the largest fragment is large, the objects in this size-range can be regenerated only in break-ups of very large parent bodies, which occur very infrequently. Hence the population in the 100m–1km range is effectively annihilated, and the cumulative size distribution has a quasi horizontal slope in this range.

Curiously, the asteroid belt does not show such a pronounced wave, and the results of CoDDEM reproduce the waves of the asteroid belt population very well (Bottke et al., 2005, 2005b). Why this is so is unclear at this stage. This may tell us that the physical nature of 1–10 km asteroids is different from that of monolithic parent bodies used in the SPH simulations of Durda et al. (2007) and Benz and Asphaug (1999). We also notice that the difference between CoDDEM and our algorithm is exacerbated in the designed experiment, because of the large collision velocities involved (almost a factor of 2 larger than in the real belt). We will do further investigations on this issue. For the moment we keep our nominal treatment of collisional fragmentation in the `Boulder` code, as the exact shape of the wave in the 100m–1km range has probably negligible effect on the accretion of large bodies, which is our primary focus.

1.4. Step *v*: Eccentricity and inclination evolution.

The evolution of eccentricities and inclinations is computed accounting for viscous stirring, dynamical friction, collisional damping, gas drag, turbulent stirring, tidal damping. We also distinguish between a large relative velocity and a low relative velocity case and consider differently the effects of isolated bodies. We treat and test all these cases below, in

sequence. Finally, we discuss the integration method used to solve these equations.

1.4.1. Viscous stirring

We follow the equations given in WS93, but with coefficients updated in Stewart and Ida (2000; SI00 hereafter) (see discussion in section II.2 of that work). More precisely we consider the following set of equations:

$$\frac{\mathrm{d}e^2(i)}{\mathrm{d}t} = \sum_j f_{ij} \frac{C_{ij}}{8} (M(i) + M(j)) e^2(i) (J_r(\beta) + 4J_\theta(\beta)) \ , \tag{14}$$

$$\frac{\mathrm{d}I^2(i)}{\mathrm{d}t} = \sum_j f_{ij} \frac{C_{ij}}{8\beta^2} (M(i) + M(j)) I^2(i) J_z(\beta) \ . \tag{15}$$

Here $\beta = [(I^2(i) + I^2(j))/(e^2(i) + e^2(j)]^{1/2}$ and the functions J_r, J_θ and J_z are given in appendix A3 of Kenyon and Luu (1999). The coefficient f_{ij} is equal to 1 if the particles i and j belong to the same annulus and otherwise it represents the fraction of particles i that intersect the volume spanned by particles j (Kenyon and Bromley, 2001; KB01 hereafter). For example, for $a(i) < a(j)$ we use:

$$f_{ij} = \frac{(a(i) + \delta a(i)/2)(1 + e(i)) - [(a(j) - \delta a(j)/2)(1 - e(j)) - N_H R_{\mathrm{Hill}}]}{2a(i)e(i) + \delta a(i)} \tag{16}$$

where N_H is a parameter equal to 2.4 if the j-bodies are non-isolated (KB01) and 6.5 otherwise (Ida and Makino, 1993), and R_{Hill} is the mutual Hill radius. The rationale behind the $N_H R_{\mathrm{Hill}}$ term is that it is not necessary to cross the orbit of a body to be stirred by it, but just to pass within a few Hill radii. Finally, the coefficient C_{ij} in eq. (14) is given by WS93:

$$C_{ij} = \frac{16G^2\rho(j)}{V_K^3 (e^2(i) + e^2(j))^{3/2}} (\log\Lambda + 0.55) \ , \tag{17}$$

where G is the gravitational constant, V_K is the Kepler velocity (computed for the arithmetic mean between $a(i)$ and $a(j)$), Λ describes the minimum two-body deflection

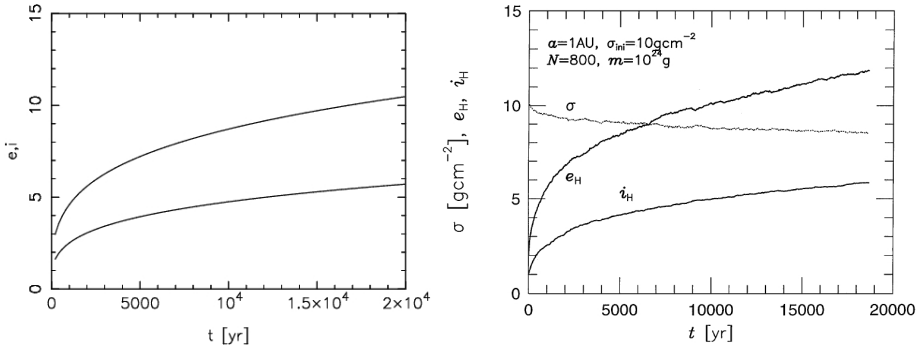

Fig. 5— Left: The evolution of eccentricity (upper curve) and inclination (lower curve) in the experiments with 800 planetesimals of 10^{24}g described in the text. The time is measured in years and e and I are expressed relative to the mutual Hill radius of the particles. Right: reproduction of Fig.2 of SI00, showing the evolution of the rms. eccentricity and inclination in N-body simulation.

angle (detailed in Wetherill and Stewart, 1989) and $\rho(j)$ is the spatial density of particles j. The spatial density, however, can become infinite if population j is in a thin layer with vanishing orbital inclinations. This singularity is only apparent, though, because in this case the particles i would spend an infinitesimal fraction of their orbital period passing through the population j. To eliminate this singularity, following KB01, we compute $\rho(j)$ by considering that the torus spanned by the particles j has an effective height of $\sqrt{2}\max[\sin(I(j)), \sin(I(i))]$. Moreover, we assume that width of the torus is equal to the width of the semi major axis bin occupied by particles j, extended at the inner and the outer radius by $a(j)e(j) + 2.4R_{\rm Hill}$. This choice is consistent with the definition of f_{ij} above.

We are aware that more modern formulations for the viscous stirring (and dynamical friction, see below) have been given in the literature (see for instance SI00; KB01; Ohtsuki et al., 2002; Ohtsuki, 2006a, 2006b), but we are seduced by the simplicity of eq. (14) and the examples illustrated below show that it is sufficiently accurate for our purposes.

As a test of the viscous stirring equations, we have considered the experiment described

in Fig. 2 of SI00 and Fig. 9 of KB01. The experiment consists in considering a population of 800 planetesimals, each of mass 10^{24}g, in an annulus centered at 1 AU with half-width of 0.028 AU. The initial eccentricity is set equal to $2R_H$ and the inclination equal to $1R_H$. Fig. 5 shows the evolution of e and I over 20,000 y. The agreement with the results of SI00 and KB01 is good (compare the left and right panels in Fig. 5). By changing the individual particle mass or surface density of the particle swarm we also recover the scaling law given in equations (5.4) and (5.5) of SI00.

1.4.2. Dynamical friction

Again, we follow the formulation of WS93, with coefficients updated in SI00, namely:

$$\frac{\mathrm{d}e^2(i)}{\mathrm{d}t} = \sum_j f_{ij} \frac{C_{ij}}{4} (M(J)e^2(j) - M(i)e^2(i))(K_r(\beta) + 4K_\theta(\beta)) \ , \tag{18}$$

$$\frac{\mathrm{d}I^2(i)}{\mathrm{d}t} = \sum_j f_{ij} \frac{C_{ij}}{4\beta^2} (M(J)I^2(j) - M(i)I^2(i))K_z(\beta) \ , \tag{19}$$

where the coefficients f_{ij} and C_{ij} are the same as in eq. (14) and the functions K_r, K_θ and K_z are given in appendix A3 of Kenyon and Luu (1999).

To test these dynamical friction equations (coupled with the viscous stirring equations above) we have attempted to reproduce the experiment described in Fig. 9a of SI00. More precisely, we have considered a bi-modal population of planetesimals made of 800 objects of individual mass equal to 10^{24}g and 200 objects of individual mass equal to 4×10^{24}g. The annulus in which they evolve is centered at 1 AU, and has a half-width of 0.056 AU. The initial eccentricities are 0.002 and the initial inclinations are 0.001 for both populations. Fig. 6 shows the evolution of e and I of both populations, over 7,000 y. The result is in agreement with that of SI00 (compare the left with the right panel in Fig. 6). We also reproduced with comparable success the experiment illustrated in Fig. 9b of SI00.

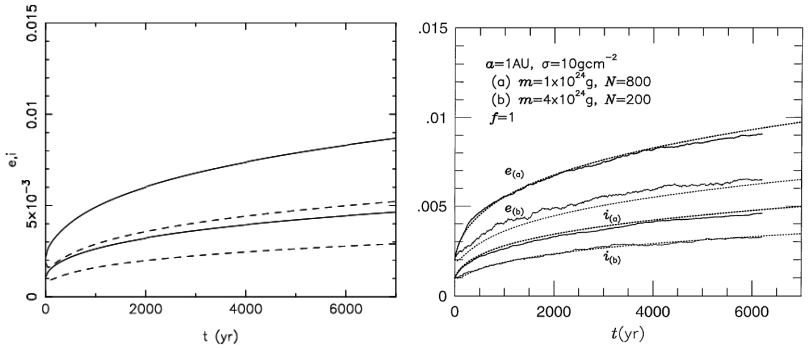

Fig. 6— Left: the solid curves show the evolution of eccentricity (upper curve) and inclination (lower curve) of the population of objects of 10^{24}g. The dashed curves show the same but for the population of objects of 4×10^{24}g. Right: reproduction of Fig.9a of SI00, where the non-smooth curves show the result of the original numerical simulation.

1.4.3. Low eccentricity case

The equations (14), (15), (18) and (19) are applied in the dispersion regime, namely when the eccentricities are larger than the non-dimensional quantity $R_{\rm Hill}/a$, as it was the case of the experiments illustrated in Fig. 5 and 6. In the opposite case, the stirring and damping rates need to be reduced (Ida, 1990; WS93). We follow the recipe given in Kenyon and Luu (1999). More precisely, we define

$$e_{lv} = \sqrt{\frac{8}{5}} R_{\rm Hill}/a \ ; \tag{20}$$

then, for $(e^2(i) + e^2(j)) < e_{lv}^2$ we compute the coefficient

$$\epsilon = \left(\frac{e^2(i) + e^2(j)}{e_{lv}^2} \right) \tag{21}$$

and we multiply the right hand side of eq. (14) by ϵ and those of eqs. (15), (18) and (19) by ϵ^2.

Again, we are aware that this is not the most modern recipe (see for instance KB01), but its simplicity is attractive and the test below, from KB01, shows that it is probably

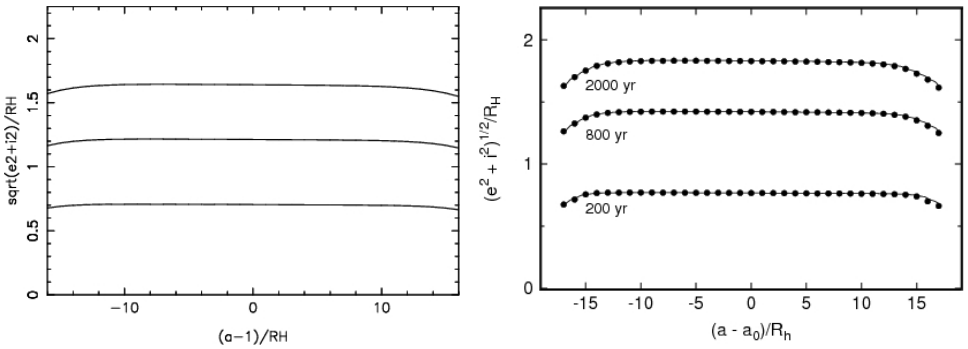

Fig. 7— Left: The value of $\sqrt{e^2 + I^2}/R_{\rm Hill}$ as a function of semi-major axis at times 200y (lower curve), 800y (middle curve) and 2,000y (upper curve), for a system of 805 particles with mass 2×10^{24}g spread over the represented ring, and initial eccentricity and inclination equal to $10^{-2} R_{\rm Hill}$. $R_{\rm Hill}$ is in this case defined as the Hill radius of a 2×10^{26}g body at 1 AU, namely 0.003235 AU. Right: reproduction of Fig. 12 of KB01, showing the same evolution according to the code in that work.

reasonable. The experiment, which also tests the capability of our code to work in a multi-annulus regime, uses 805 planetesimals with individual masses equal to 2×10^{24}g, in a ring from 0.9434 to 1.0566 AU, subdivided in 35 annuli. The initial eccentricity of the particles, equal to the initial inclination, is 3.235×10^{-5}, which is 27 times smaller than their mutual Hill radius (so that, initially, the system is in the low-velocity regime). Fig. 7 shows $\sqrt{e^2 + I^2}$ at $t = 200$y, $t = 800$y and $t = 2000$y in each of the annuli. The figure compares quite well with the results of KB01 (compare the left with the right panel in Fig. 7). Our disk is slightly less excited than that in the simulation of KB01, and the bending of the curves at the extremes of the disk is a bit less pronounced.

1.4.4. Isolated bodies

In the evaluation of viscous stirring and dynamical friction, a somewhat different treatment is followed when the population j is made of isolated bodies. For reference, the definition of isolated body is given in sect. 1.1. Below we first describe how we account for the effects of isolated bodies on non-isolated bodies and then of isolated bodies on themselves.

(a) Effects on non-isolated bodies

Let's consider the case where the particles i, interacting with the isolated bodies j, are themselves non-isolated. Following WS93, we assume that the particles interact only with one object, chosen at random in the list of isolated bodies in the annulus. The rationale behind this is that, because the isolated bodies are separated from each other, a small body can only interact closely with a single isolated body at a time.

In the computation of the effects of a single massive object, we encounter a problem. The 'spatial density', which enters in eq. (17), has in principle no meaning in this case. This issue is explicitly discussed in Ida and Makino (1993). After some tests, we decided to compute an effective spatial density by considering that the mass of the object is spread over an annulus of width $\pm 2.4 R_{\rm Hill}$ around its orbit. As for the height of the torus, again we consider the $\max[\sin(I(i), \sin(I(j))]$. Numerical simulations (see for instance Ida and Makino, 1993) also show that massive bodies are much more efficient in stirring the eccentricities than the inclinations of the small bodies than eqs. (14) and (15) would predict. For this reason, we divide the right hand side of eq. (15) by a factor of 6. For reference, in the analytic formulation of Ida and Makino, the numerical coefficient in the equation for the viscous stirring of the inclination is 20 times smaller than the one in the equation for the viscous stirring of the eccentricity (in our case the above-mentioned factor

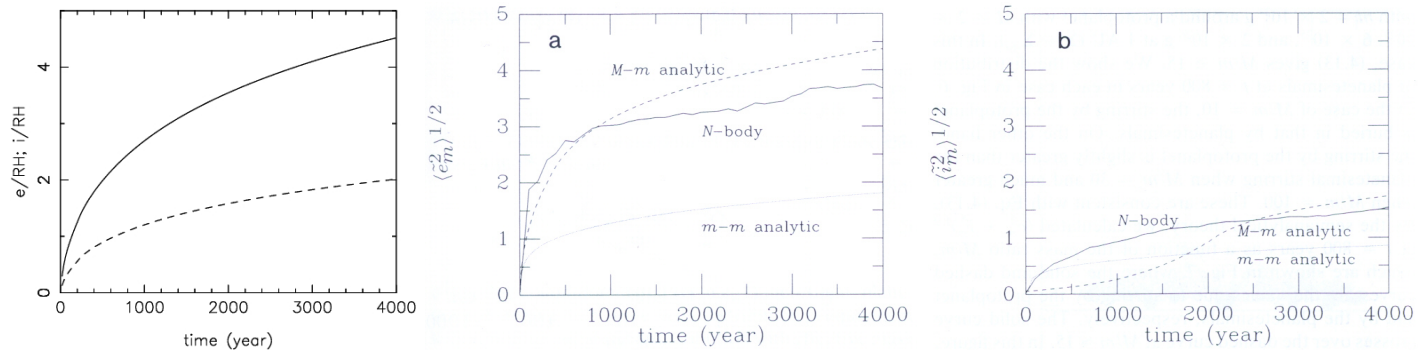

Fig. 8— Left: the time evolution of the eccentricity (solid) and inclination (dashed) of the particles with $1 - 5R_{\rm Hill} < a < 1 + 5R_{\rm Hill}$, when a body of 2×10^{26}g is taken introduced at 1 AU in the disk considered in Fig. 7. Center and Right: reproduction of Fig. 5 of Ida and Makino (1993), where the non-smooth curves show the result of the N-body simulation in that work.

of 6 is multiplied by $[J_r(\beta) + 4J_\theta(\beta)]/J_z(\beta)$, which is 1-3, depending on the value of β).

We test the effectiveness of this recipe by trying to reproduce the result of the simulation reported in section III.2 in Ida and Makino (1993), which is also addressed in KB01 (see Fig. 13 in that work). The experiment consists in considering a particle disk as in the case of Fig. 7, but with a body of 2×10^{26}g added at 1 AU. Fig. 8 shows the time evolution of the eccentricities and inclinations of the particles in the region within $\pm 5R_{\rm Hill}$ of the massive body. Our result agrees satisfactorily with the result of the N-body simulation in Ida and Makino (1993) (compare the left panel with the center and right panels of Fig. 8).

Fig. 9 shows the excitation distribution in the disk at times 200, 800 and 2,000 years. It also agrees quite well with what is measured in the numerical simulation of Ida and Makino (1993) (compare the left with the right panels). Obviously, our aim here is not to reproduce the fine structure showed in the histograms of the right panels of Fig. 9, but rather the broad structure of the disk's excitation, highlighted by the dashed lines in the right panels.

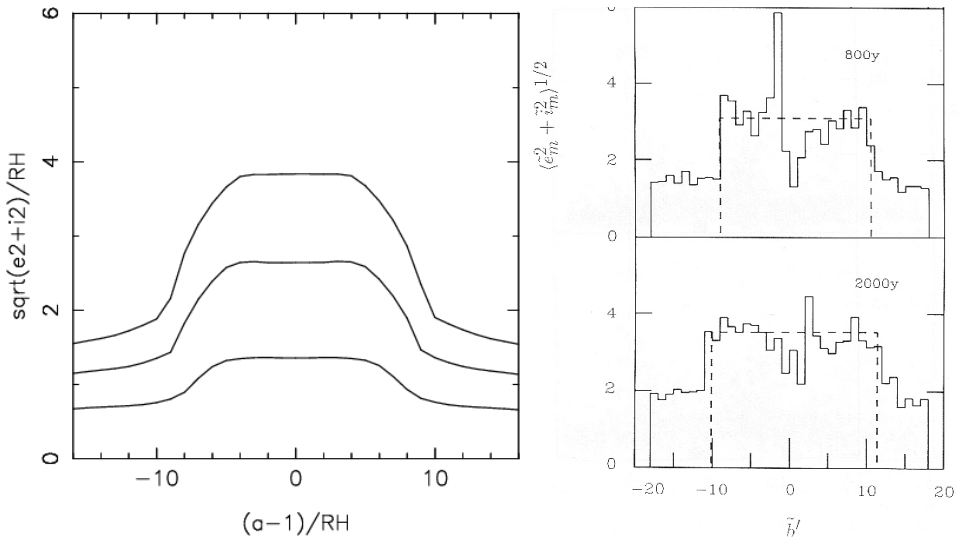

Fig. 9— Left: the same as the left panel of Fig. 7, but a body of 2×10^{26}g is taken into account 1 AU. Right: reproduction of Fig. 4 of Ida and Makino (1993), showing the excitation measured in the disk at times 800y and 2000y in the N-body simulation.

In conclusion, our treatment of the stirring effect of an isolated body on small bodies seems to be reasonable for both what concerns the magnitude of the excitation and its localization in the disk.

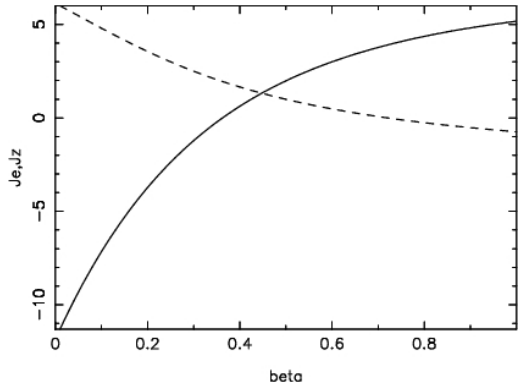

Fig. 10— Solid curve: the value of $J_e \equiv J_r(\beta) + 4J_\theta(\beta)$ as a function of β. Dashed curve: the value of $J_z(\beta)$.

(b) Effects of the isolated bodies on themselves.

In this case, we use essentially the same recipe that we followed for computing the effects on the small bodies, but with some amendments. We consider that each isolated body interacts (mainly) only with its closest neighbor. So, as for the small bodies, we assume that each isolated body interacts only with a single object, chosen at random in the list of the remaining isolated bodies in the annulus. If there are no remaining isolated bodies (i.e. the isolated body in consideration is alone in its own annulus), we choose an isolated body in the annulus with which the interaction is the strongest, according to value of the coefficient f_{ij} defined in eq. (16). Moreover, because isolated bodies, by definition, avoid close encounters with each other, in the interaction between two isolated bodies we consider only the 'distant effects', as suggested by WS93. This is done by considering the standard equations for viscous stirring and dynamical friction, but imposing $\Lambda = 1$ in eq. (17).

In most applications, the isolated bodies tend to have very small eccentricities and inclinations, because they are damped by the the dynamical friction exerted by the planetesimal disk. Numerical simulations show that massive bodies on quasi-coplanar orbits

tend to excite much more efficiently their own eccentricities than their own inclinations. In our formulae this is reflected by the fact that, at low relative velocity, the right hand side of eq. (14) is multiplied by ϵ (see eq. 21), whereas the right hand side of eq. (15) is multiplied by ϵ^2. However, according to eqs. (14) and (15) the eccentricities cannot be excited much faster than the inclinations. In fact, if this were the case, the coefficient β (essentially $\sim I/e$) would become small. But, as Fig. 10 shows, for $\beta < 0.36$ the term $J_r(\beta) + 4J_\theta(\beta)$ is negative. Thus, eq. (14) would become a *damping equation*, preventing further growth of the orbital eccentricity. In other words, the eccentricity has to 'wait' for the inclination to grow, in order to be able to grow as well. This is in sharp contrast with what numerical simulations show (see Fig. 11). To overcome this problem, whenever β decreases below 0.37, we assume that it is equal to this value when computing $J_r(\beta) + 4J_\theta(\beta)$ in eq. (14). This essentially decouples the evolution of eccentricity and inclination.

To test this recipe, we have done a N-body simulation of two systems of 'planets'. The first system is made of three objects with individual mass equal to 10^{27}g, placed at 28.5, 30.5 and 32.5 AU. Their initial eccentricity is equal to 10^{-4} and their initial inclination is half of this value. The angles M, Ω, ω have been chosen at random. The second system is made of 10 objects with individual mass equal to 5.23×10^{26}g, placed at 1 AU from each other starting from 25.5 AU. Their initial eccentricity is equal to 3×10^{-4} and the inclination is half of this value. Again, the orbital angles are chosen at random. We have integrated both systems for 3,000 y. The time evolution of the rms. of their eccentricities and inclinations are shown in Fig. 11 (solid curves). Notice how the rms. of the inclination is constant in both simulations. We have then used the `Boulder` code to estimate the growth of the eccentricities and inclinations in these systems. These simulations have been done with a multi-ring approach, placing each planet as a single body in its own ring. Our results are shown as dashed curves in Fig. 11. The eccentricity excitation agrees well with what is observed in the numerical simulations. The `Boulder` code, though, predicts

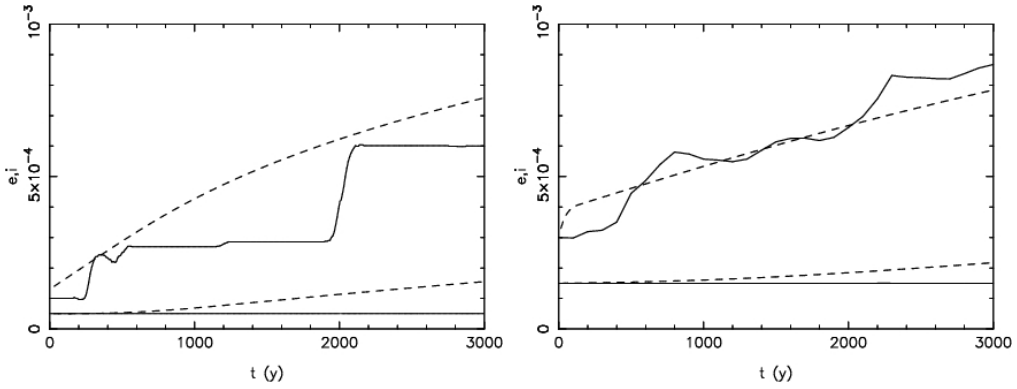

Fig. 11— Solid lines: the evolution of the rms. of the eccentricities (upper curve) and of the inclinations (lower curve) according to a N-body simulation. Dashed lines: the same, but according to the `Boulder` code. The left panel refers to the system of 3 planets and the right panel to the system of 10 planets.

some (small) excitation of the inclinations which is not seen in the N-body simulations on this timescale. The reason is that, as the eccentricity grows β decreases, and this in turn enhances the term $J_z(\beta)$ in eq. (15), as showed in Fig. 10. So, the growth of the eccentricity entails some growth of the inclination. We believe that this is not a serious problem. A moderate stirring of the inclinations of an isolated body will not affect the velocity of encounters with the planetesimals in the disk (which is dictated by the eccentricity of the isolated body and the velocity dispersion of the planetesimals), nor the encounter rate and the planetesimal stirring rate (because the volume density calculations in the respective formulae are dominated by the inclination of the planetesimals, typically much larger than that of the isolated body).

Notice also that we have chosen to do this comparison on a short timescale. On a longer timescale, the evolutions in the N-body simulation and in the `Boulder` code inexorably diverge. Planets can become unstable and very excited (this happens in the 10 planets system at 250,000 y; up to this time the eccentricity excitation predicted by the `Boulder` code still agrees quite well with the N-body simulation). Or the planets can be in a stable,

quasi-periodic motion, in which case the rms. eccentricity and inclination stop growing (this happens in the 3 planets system, after ~ 3000 y). Both phenomena cannot be reproduced by the `Boulder` code because of the very statistical nature of the code. We think, however, that the reported tests are significant, because what is important is that the `Boulder` code reproduces the *initial stirring rates*, from quasi-circular and co-planar orbits. In fact, in a full system comprising isolated bodies and a planetesimal disk, the disk would tend to drive the isolated bodies towards circular and co-planar orbits through dynamical friction; the isolated bodies would fight against this damping through their self-stirring. The equilibrium values of eccentricities and inclinations of the isolated bodies would then depend on their self-stirring rates in the vicinity of $e = I = 0$, which are what we tested above.

Below, we will consider the evolution of the same systems of 'planets' in disks affected by a strong collisional damping.

1.4.5. Collisional damping

For collisional damping we use formula (21) in Wetherill and Stewart, 1989), but with the more intuitive coefficient taken from the recent work of Goldreich et al. (2004). In practice our equations are:

$$\frac{\mathrm{d}e^2(i)}{\mathrm{d}t} = \sum_j A_{ij} \frac{M(j)(e^2(i) - e^2(j)) + 2M(i)e^2(i)}{(M(i) + M(j))^2} \ , \tag{22}$$

$$\frac{\mathrm{d}I^2(i)}{\mathrm{d}t} = \sum_j A_{ij} \frac{M(j)(I^2(i) - I^2(j)) + 2M(i)I^2(i)}{(M(i) + M(j))^2} \ , \tag{23}$$

where $A_{ij} = N(j)M(j)P_{\mathrm{int}}(i,j)F_g(i,j)(R(i) + R(j))^2$ and P_{int} and F_g are the intrinsic collision probability and focusing factor defined in eq. (1) and eq. (8), respectively.

To test these formulae, we have compared our results with those of Levison and Morbidelli (2007; LM07 hereafter), which presented a N-body code that self-consistently

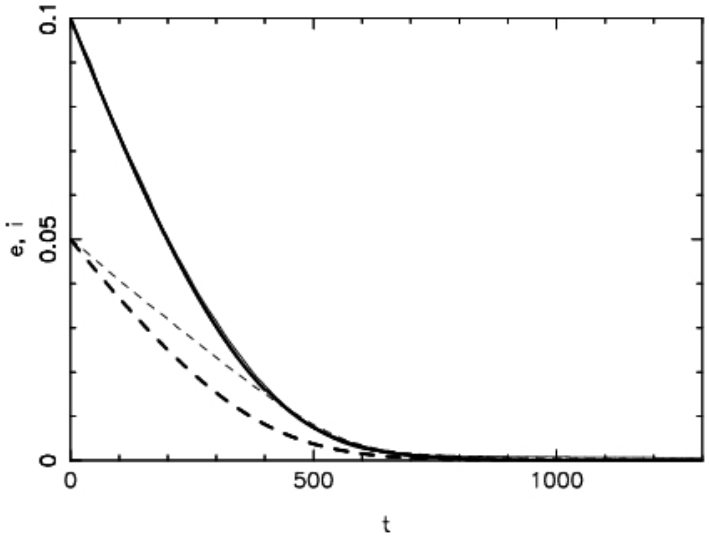

Fig. 12— The time evolution of the eccentricity (solid) and inclination (dashed) of 1.4×10^{28} particles with a radius of 1cm and a mass of 4.18g, between 30 and 35 AU, due to their mutual collsional damping. The bold curves illustrate the result from the `Boulder` code. The light curves those from Levison and Morbidelli (2007). The light and bold solid curves almost perfectly overlap, so that only one solid line is visible.

computes collisional damping. We repeated the experiment illustrated in Fig. 1 of that work, which consists in considering a ring of 1-cm-sized planetesimals between 30 and 35 AU with initial eccentricity equal to 0.1 and initial inclination equal to 0.05. The total mass of this planetesimal ring is 10 Earth masses; the bulk density of the particles is $1\mathrm{g/cm}^3$.

Fig. 12 compares our result (bold curves) with that of LM07 (light curves). Solid curves are for eccentricity and dashed curves for inclination. The evolution of the eccentricity in our simulation is indistinguishable from that of LM07 (so, the reader sees only one solid curve in the figure). The damping of the inclination is faster in our case than in LM07, but not by too much. The e-folding time in our case is 265 y, whereas it is 360 y in LM07.

Two interesting experiments were also shown in LM07, concerning the systems of planets considered in Fig. 11, embedded in particle disks undergoing strong collisional

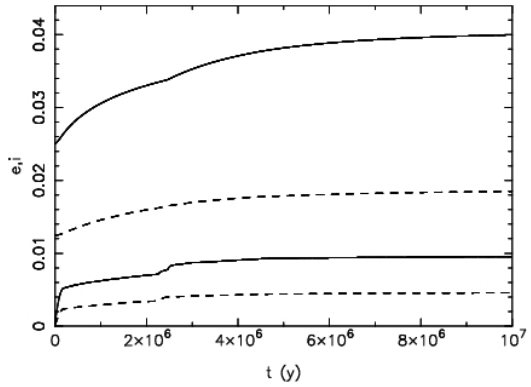

Fig. 13— The time evolution of the mean eccentricity (solid) and inclination (dashed) of the system of 10 massive bodies embedded in a disk of 100 m bodies as in the simulation of Fig. 3 of LM07. The initial set-up is discussed in the text. The upper curves refer to the small bodies; the lower curves to the massive bodies. Compare with Fig. 3 of LM07.

damping. More precisely, the 10 planets system is embedded in a disk of 100 m bodies, ranging from 20 to 40 AU, carrying cumulatively a mass of 3.39×10^{28} g. The initial mean eccentricity and inclination of the particles are 0.025 and 0.0125, respectively. Fig. 13 shows the result of our simulation, obtained using 20 annuli, each of width equal to 1 AU. The upper curves show the evolution of the mean eccentricity (solid) and inclination (dash) of the planetesimals. The lower curves are the same but for the 10 massive bodies. The excitation of the small bodies reaches ~ 0.04 in eccentricity and ~ 0.02 in inclination in 10^7 y. In the simulation of LM07 (see Fig. 3 in that paper) the final values are ~ 0.035 and 0.018 respectively. In Goldreich et al. (2004), the expected eccentricity excitation of the small bodies is also ~ 0.04. As for the massive bodies, Goldreich et al. predict mean $e \sim 0.008$ and mean inclination that is half of this value. We find 0.010 and 0.0045 respectively. In the simulations of LM07, the results depend quite sensitively on the number of tracers used to represent the particle disk. The values that we have found for the final excitation of the planets are within the range spanned by those simulations, although the run in LM07 with the largest number of tracers gives final excitations that are about half

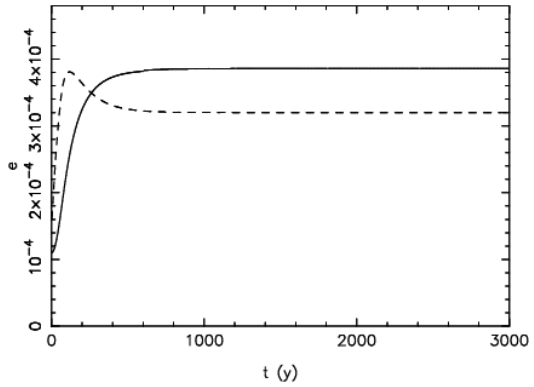

Fig. 14— The time evolution of the mean eccentricity of a system of 3 massive embryos (dashed curve) embedded in a disk of 5 cm bodies (solid curve) as in the simulation of Fig. 4 of LM07. The initial set-up is discussed in the text. Compare with Fig. 4 of LM07.

of ours.

The second experiment in LM07 consists in embedding the 3 planets system considered before in a 7 $M_\oplus$ disk of planetesimals spread from 27 to 33 AU. The size of the planetesimals is 5 cm, and their bulk density is 1g/cm^3. The initial eccentricities and inclinations are 1×10^{-4} and 0.5×10^{-4} respectively, for both embryos and small bodies. The results of our simulations are shown in Fig. 14, obtained using 6 annuli, each of width equal to 1 AU. The dashed curve shows the mean eccentricity of the embryos and the solid one shows that of the small bodies. At the end of our 3,000 y simulation we find that the mean eccentricity of the embryos is $3.2{\times}10^{-4}$ and the one of the small bodies is 4×10^{-4}. According to Goldreich et al. (2004), these values should be 7×10^{-4} and 2×10^{-4}. In the simulation of LM07 (see Fig. 4 in that work), the final excitation of the disk is $e \sim 4 \times 10^{-4}$. For the embryos, again, there is a strong sensitivity on the number of tracers used to model the disk in LM07. The simulations with the largest number of tracers give a final mean eccentricity of 8–$10{\times}10^{-4}$. However, a visual inspection of the evolution of the planets and planetesimals in the simulation of LM07 shows that the excess of excitation that the planets get with respect to a simulation without the disk (left panel of Fig. 11) is due to the fact

that the planetesimals, under their strong mutual collisional damping, clump in narrow structures in the tadpole regions and in the mean motion resonances of the planets, and then behave coherently almost as a unique massive body. This behavior, of course, cannot be captured by the `Boulder` code, because phase mixing is an essential assumption behind all the stirring/damping equations that we have used. In any case, the values obtained by the `Boulder` code, by Goldreich et al. (2004) and LM07 are all in the same ballpark. Given the extreme character of this experiment, we consider this to be a success of our code.

1.4.6. Gas drag

From formula (23) of Wetherill and Stewart (1989), our equations for gas drag damping on eccentricity and inclination are:

$$\frac{\mathrm{d}e^2(i)}{\mathrm{d}t} = -\frac{16}{5}\frac{V}{V_K^2}\frac{0.5\pi\rho_g V_g^2 R^2(i)}{2M(i)(1+0.8\beta^2)} \ , \tag{24}$$

$$\frac{\mathrm{d}I^2(i)}{\mathrm{d}t} = -3.2\beta^2\frac{V}{V_K^2}\frac{0.5\pi\rho_g V_g^2 R^2(i)}{2M(i)(1+0.8\beta^2)} \ , \tag{25}$$

where $V = V_K\sqrt{(5/8e^2(i) + 1/2I^2(i))}$ is the velocity of the planetesimal relative to the local Keplerian velocity and $V_g = \sqrt{V(V+\delta V)}$ is the gas velocity. The quantity δV, the difference between the gas and the Kepler velocity, is assumed to be 60m/s for $a < 5$ AU (see WS93). The volume gas density is denoted by ρ_g. We have tested these formulae against a N-body code with gas-drag forces, obtaining identical results.

For the moment, we neglect in the `Boulder` code the radial migration of planetesimals induced by gas drag, implicitly assuming that what moves away from an annulus is replaced by new material coming in from further out.

1.4.7. Turbulent stirring

It is now quite generally accepted that proto-planetary gas disks are turbulent due to a Magneto Rotational Instability (MRI). For a few years, the dynamics of objects in turbulent disks has been studied through very CPU-expensive magneto hydro-dynamical simulations (see for instance Nelson et Papaloizou, 2004; Nelson, 2005). Turbulence turns out to have two effects on solid bodies. It forces them to have a stochastic, random-walk migration in semi major axis, and it also excites their eccentricity and inclination. A synthetic recipe for implementing in a numerical code the stochastic torques exerted by a turbulent disk on planetesimals and proto-planets was formulated in Laughlin et al. (2004). This recipe was implemented in Ida et al. (2008) and from the numerical simulations, a simple formula was deduced for the growth of the eccentricity in a turbulent regime. From that formula, we derive an equation for $\mathrm{d}e^2/\mathrm{d}t$ that we adopt in our code:

$$\frac{\mathrm{d}e^2(i)}{\mathrm{d}t} = 0.01 f_g^2 \gamma^2 \left(\frac{1\mathrm{AU}}{a(i)}\right)^{1/2} , \tag{26}$$

where f_g is related to the surface density of gas Σ_g by the equation $\Sigma_g = 2400 f_g (r/1\mathrm{AU})^{-3/2}$ (so that $f_g = 1$ gives a density corresponding to 1.4 times the minimal mass solar nebula), and γ is a non-dimensional parameter to represents the 'strength of the turbulence'. Reasonable values for γ are between 10^{-4} and 10^{-2}, according to MRI simulations (Ida et al., 2008).

The evolution of the inclination is not explicitly studied in Ida et al. (2008), but considering that typically the inclination follows the evolution of the eccentricity in order to keep a ratio $e/I \sim 2$, we set:

$$\frac{\mathrm{d}I^2(i)}{\mathrm{d}t} = 1/4 \frac{\mathrm{d}e^2(i)}{\mathrm{d}t} , \tag{27}$$

where $\mathrm{d}e^2(i)/\mathrm{d}t$ is given by eq. (26)

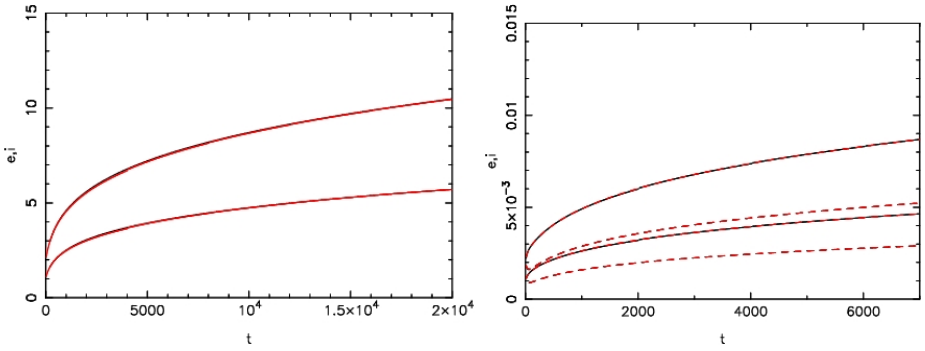

Fig. 15— Comparison between the Euler method and the Shampine and Gordon ODE solver for the eccentricity/inclination evolution equations. The black curves show the results of the experiments already illustrated in Figs. 5 and 6 (Euler method). The red curves show the results of the same experiments obtained with the Shampine and Gordon solver. The match is so good that the black curves are barely visible.

1.4.8. Solution of the eccentricity/inclination equations

In all the experiments illustrated above, the eccentricity/inclination equations have been solved using an Euler method, e.g. for each particle i

$$e^2(t+\mathrm{d}t) = e^2(t) + \mathrm{d}t \frac{\mathrm{d}e^2(i)}{\mathrm{d}t}(t) \ , \quad I^2(t+\mathrm{d}t) = I^2(t) + \mathrm{d}t \frac{\mathrm{d}I^2(i)}{\mathrm{d}t}(t) \ . \tag{28}$$

The time-step $\mathrm{d}t$ is chosen in an adaptive manner, so that e and I for all particles do not change more than a parameter value, which was set equal to 10% for all our simulations.

It may be of concern that the Euler method might not be accurate enough. To check this, we wrote a modified version of the `Boulder` code, in which the differential equations for the evolution of e^2 and I^2 are solved using a predictor-corrector integrator, known as the Shampine and Gordon ODE solver (Shampine and Gordon, 1975). The absolute and relative tolerance used in this integration method have been set equal to 10^{-10}.

Fig. 15 compares the new results with those obtained with the Euler method, for the experiments already illustrated in Figs. 5 and 6. The match with the previous solutions is

essentially perfect. The reason for this is that the equations for the evolution of eccentricity and inclination are not hyperbolic and the adaptive time-step used in the Euler-method solution was set in a conservative way.

In the complete version of the `Boulder` code (e.g. in that accounting not only for the eccentricity/inclination evolution, but also for coagulation and fragmentation) we prefer to use the Euler method instead of a more sophisticated integration scheme for one simple reason. The coagulation/fragmentation algorithm is not written in the form of differential equations. Thus the evolution of the mass distribution cannot be computed using a differential equations integrator. Using the simple Euler algorithm, we use the same time-step for both the coagulation/fragmentation algorithm and the eccentricity/inclination evolution equations. In this way the mass distribution is updated every time that the right hand sides of the eccentricity/inclination equations are evaluated. If we used a more sophisticated integrator for the eccentricity/inclination equations, the internal time-step used by the integrator would be unrelated with that used in the coagulation/fragmentation algorithm and the mass distribution wouldn't be updated at each intermediate sub-step that the integrator takes. This inconsistency could lead eventually to *less* accurate results.

1.5. Step *vi*: Dynamical definition and allocation of mass bins.

At the end of each time-step, after all the calculations described above, the `Boulder` code proceeds to a re-arrangement of the mass bins. The first operation is the re-definition of the mean value of the mass in each bin, by dividing the total mass by the total number of objects. This operation is very important, otherwise objects could grow (shrink) only if they accrete (shed) enough mass in a time-step to jump from one bin to another.

As bins are re-defined at the end of the time-step, four situations can occur:

(i) the ordering of the bins is no longer monotonic in the mean bin mass. In this case, all bins are re-sorted.

(ii) The mean mass of a bin can become smaller than the minimum mass m that is tracked in the code. In this case the bin is deleted and we lose track of its population.

(iii) The mean masses of two bins can become too close to each other, so that their ratio is less than $\sqrt{\delta m}$. In this case the two bins are joined. The populations in two bins are summed up. For the eccentricity and inclination we adopt the mass weighted mean of the values of the two bins.

(iv) The mean masses of two bins can become too far from each other, so that their ratio is larger than $(\delta m)^{3/2}$. In this case, one or several new bins are generated between the two. If the mean mass of a new bin is 'close' to the minimal mass m, typically within a factor of 10, we fill the new bin by interpolation of the quantities (total mass, number of objects, eccentricity, inclination) carried by the neighboring bins. The populations in the neighboring bins are reduced by an appropriate factor, in order to ensure the conservation of mass and population number during this operation. We do this because it is dangerous to have strong discontinuities in the tail of the population mass distribution. For instance, when (if) bin # 1 is eliminated because it becomes smaller than the minimum tracked mass m, bin # 2 is renamed bin # 1. If its content is very different from that of the former bin # 1, the extrapolation of the size distribution between masses μ and m, which is anchored to bin # 1 (see below), would suffer a sudden change, with possible dramatic effects on the full size distribution of the population. Conversely, we leave the bins empty if their mean mass is much larger than m. This is important in case of runaway growth. When a single body grows faster than the rest of the population, new bins need to be generated in between the bin of the runaway body and the bins carrying the rest of the planetesimals. These bins must be empty, otherwise the very nature of runaway growth would be modified.

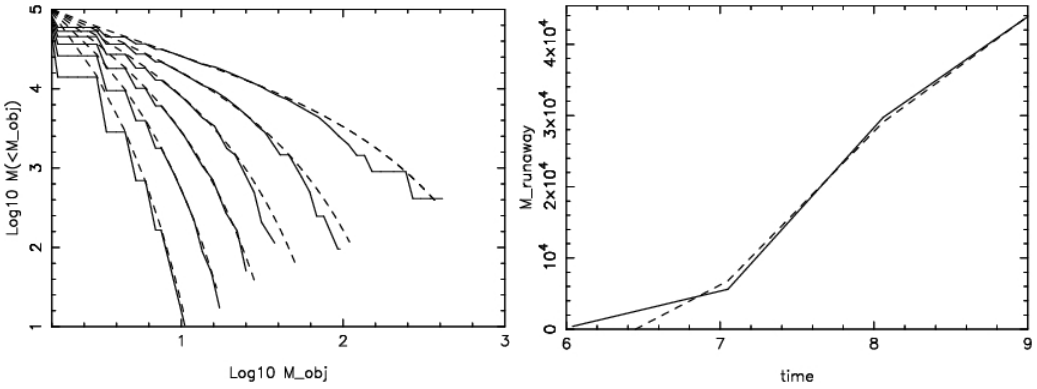

Fig. 16— Left: the cumulative mass distribution resulting from our simulation (solid lines) and expected from analytic calculations (dashed curves). From left to right, the curves are given for times $t = 1$ to $t = 6$, which correspond to $\eta = 0.15$ to 0.9. Right: the mass of the largest (runaway) body as a function of time. The solid line represents the result of our simulation and the dashed curve the analytic expectation. The units are arbitrary (see text).

To test the ability of our moving bin algorithm to follow the evolution of the mass distribution of a planetesimal population, and runaway growth in particular, we have considered the academic case in which the collision probability between two bodies of masses $M(i)$ and $M(j)$ is simply $10^{-6}M(i)M(j)$ (Wetherill, 1990; Kenyon and Luu, 1998). The simulation starts with N_1 =66,666 bodies of mass M_1 =1.5 (the unit is arbitrary). This model triggers runaway growth at a time t such that $\eta = 10^{-6}N_1 t = 1$. For $\eta < 1$ there is an analytic solution for the mass distribution of the population, reported in formula A35 of Kenyon and Luu (1998). For $\eta > 1$ there is a formula for the mass of the runaway body, reported in formula A36 of Kenyon and Luu (1998). Fig. 16 compares the result of our code to these analytic solutions. The mass distribution of the population (solid curves) follows the expected solution (dashed curves) quite well. Deviations can be seen at the low mass range, due to the effects of bin discretization, and at the large mass range (due to small number statistics on the populations of objects in the most massive bins), but the trend of the evolution of the mass distribution is reproduced satisfactorily. The growth of the

runaway body is also reproduced very well.

We finally discuss the issue of the generation of a distribution of objects with masses between μ and m by extrapolation of the size distribution observed at masses larger than m. We first compute the impact velocity among objects in the first bin of the mass distribution. Given this speed, we compute the minimal mass of a projectile that is capable of disrupting catastrophically a body in the first mass bin. μ is defined as a tenth of that minimal mass. Then, we assume that the size distribution of bodies with masses between μ and m is

$$N(r)\mathrm{d}r = N_0 r^{-q}\mathrm{d}r \ . \tag{29}$$

The exponent q is set equal to the one measured for the current size distribution between bin # 1 (the closest to m) and a bin with a mean mass close to $10^3 m$. This choice is done in order to span an order of magnitude in size, thus achieving a quite stable estimate of q with respect to small fluctuations of the populations in the bins. If this is not possible (for instance the population has not yet evolved to $10^3 m$, the exponent q is assumed to be equal to 3.5, the value for the equilibrium size distribution in Dohnanyi (1969). Once q is set, the coefficient N_0 in eq. (29) is computed in such a way that the integral

$$\int_{r_m(1)}^{r_M(1)} N(r)\mathrm{d}r = N(1) \ , \tag{30}$$

where $N(1)$ in the population number in bin # 1 and $r_m(1)$ and $r_M(1)$ are the minimum and maximum radius defining the bin.

1.6. Testing the code as a whole.

Up to now we have tested individually single parts of the code. To test the performance of the code as a whole, in all its complexity, we now consider the experiment described in WS93. The experiment starts with a population initially made of 8.33×10^8 planetesimals

of individual mass equal to 4.8×10^{18}g and bulk density equal to 3g/cm^3, placed in an annulus centered at 1 AU with width 0.17 AU, and a velocity dispersion relative to the Keplerian orbit of 4.7m/s.

For a more direct comparison with the results of WS93, we have modified our code to make it as similar as possible to the original code of WS93. In particular, we have changed the coefficients of the viscous stirring and dynamical friction equations, we have changed the threshold for transitioning from the small to the large velocity regime and the treatment of the low velocity case. Moreover, because WS93 does not talk explicitly about it, we understand that the volume density $\rho(j)$ entering in the calculation of the coefficient (17) of the viscous stirring and damping equations, was calculated in WS93 using as scale height the sine of the inclination of the particles j, rather than $\max[\sin(I(j)), \sin(I(i))]$ (see section on viscous stirring). So, we have done the same for this test. Finally, because the treatment of fragmentation in our code is very different from the code in WS93, we have not taken into account fragmentation, as in the simulation illustrated in Fig. 12 of WS93.

The top left panel of Fig. 17 shows our result. Several aspects are very similar to the original result in WS93. The mass of the largest objects as a function of time is almost identical. The shape typical of runaway growth, with a gap in mass between the group of isolated bodies and the rest of the distribution, develops at 50,000 y in both simulations. The total number of isolated bodies is also in agreement, as well as the number of the smallest bodies. The most striking difference is that at the end of the simulation the gap in mass between the isolated bodies and the rest of the distribution is one order of magnitude larger in our case than in WS93. This is due to the fact that the velocity distribution in our simulation presents a steeper anti-correlation with the mass of the bodies than in WS93, for masses larger than 10^{22}–10^{23}g. This anti-correlation is due to dynamical friction, and it is not clear to us why it was so shallow in WS93. Then, because the bodies with mass

10^{22}–10^{23}g are on orbits that are more circular and less inclined than in WS93, they are swallowed more easily by the isolated bodies, due to the enhanced gravitational focusing factor. This results in the disappearance of these bodies in our simulation and hence in the formation of a wider mass gap in the final distribution.

The top right panel of Fig. 17 shows the result of the same simulation, when our nominal code is used (i.e. without the changes introduced to try to reproduce the code of WS93, but still without fragmentation). Two effects occur with respect to the previous simulations, that explain the differences in the results. First, because the transition from the low velocity regime to the large velocity regime now occurs at smaller eccentricities, and the treatment of the low velocity case is now less extreme than in WS93, the planetesimals are excited faster. This in principle would slow down accretion. It would also reduce the gap between the isolated bodies and the most massive non-isolated bodies because the latter, more excited in eccentricity, would be less easily accreted by the isolated bodies. Second, because in the definition of the volume density $\rho(j)$ in eq. (17) we now account also for the inclination of particles i, the stirring of the small bodies by the big bodies is reduced relative to the previous simulation. This boosts accretion. The net result is that accretion happens faster than in the previous simulations; the largest bodies produced in 150,000 y are now about twice more massive than before; there is almost no gap in mass between isolated and non-isolated bodies, so that the final mass distribution is smoother than before, although still very shallow in the 10^{24}–10^{26}g range. Curiously this last aspect is in better agreement with that found in WS93 and, particularly, in Kenyon and Luu (1998).

The central panel of Fig. 17 shows the result of a simulation where fragmentation is also taken into account. The scale on the abscissa is the same as in the top panels, to help comparison, but the range of masses now spans a much larger interval, because bodies smaller than the initial mass of 4.8×10^{18}g are produced by collisional fragmentation.

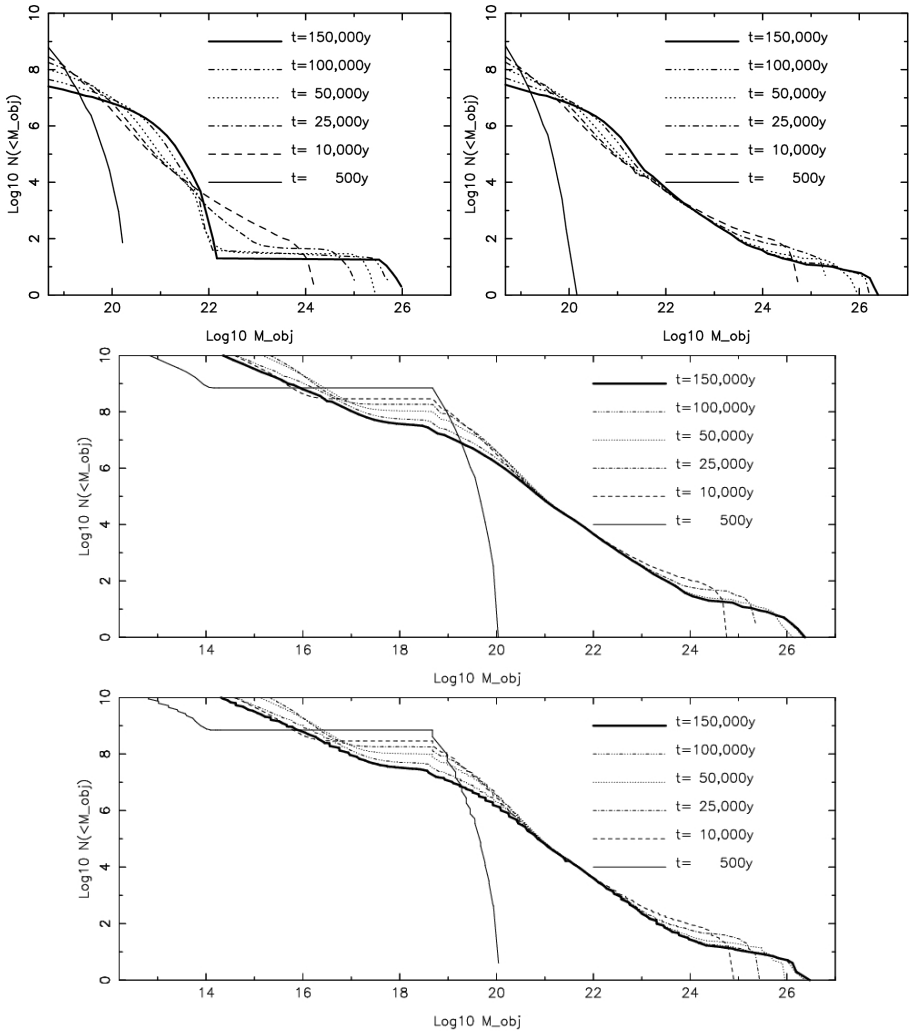

Fig. 17— The cumulative mass distribution at progressive times, starting from a population of 8.33×10^8 planetesimals of 4.8×10^{18}g, between 0.915 and 1.085 AU. Top left: our result when we try to follow as best as we can the prescriptions in WS93; compare with Fig. 12 of WS93 and/or Fig. 1 of Kenyon and Luu (1998); no fragmentation is taken into account. Top right: the same, but with our preferred equations for the velocity evolution; still no fragmentation is taken into account. Center: now accounting also for fragmentation. Bottom: the same as the central panel, but the simulation is made dividing the systems in two rings, instead of in a single-ring mode.

Overall we find that the role of fragmentation is quite negligible for the accretion of the largest bodies. A similar conclusion was also reached in WS93. The final mass distribution, however, changes considerably in the range 10^{19}–10^{21}g, because bodies in this mass range are effectively eroded by collisions, so that their number *decreases* relative to the distributions at earlier times, rather than *increasing* as it does in the top panels.

The bottom panel of Fig. 17 shows the result of the same simulation, but performed by subdividing the system in two annuli (in the previous simulations of this test we used a single annulus approach). The differences with the results shown in the central panel are negligible and probably just due to the moderately stochastic aspect of accretion. This shows that the `Boulder` code as a whole works correctly also in a multi-annuli regime.

REFERENCES

- Agnor, C., Asphaug, E. 2004. Accretion Efficiency during Planetary Collisions. *Astrophysical Journal* 613, L157-L160 (2004).
- Benz, W., Asphaug, E. Catastrophic Disruptions Revisited. *Icarus* 142, 5-20 (1999).
- Bottke, W. F. et al. The fossilized size distribution of the main asteroid belt. *Icarus* 175, 111-140 (2005).
- Bottke, W. F. et al. Linking the collisional history of the main asteroid belt to its dynamical excitation and depletion. *Icarus* 179, 63-94 (2005).
- Dohnanyi, J. W. Collisional models of asteroids and their debris. *Journal of Geophysical Research* 74, 2531-2554 (1969).
- Durda, D. D. et al. Size frequency distributions of fragments from SPH/N-body simulations of asteroid impacts: Comparison with observed asteroid families. *Icarus*

186, 498-516 (2007).

- Greenberg, R., Bottke, W. F., Carusi, A., Valsecchi, G. B. Planetary accretion rates - Analytical derivation. *Icarus* 94, 98-111 (1991).

- Greenzweig, Y., Lissauer, J. J. Accretion rates of protoplanets. *Icarus* 87, 40-77 (1990).

- Greenzweig, Y., Lissauer, J. J. Accretion rates of protoplanets. II - Gaussian distributions of planetesimal velocities. *Icarus* 100, 440-463 (1992).

- Goldreich, P., Lithwick, Y., Sari, R. Final Stages of Planet Formation. *Astrophysical Journal* 614, 497-507 (2004).

- Ida, S. Stirring and dynamical friction rates of planetesimals in the solar gravitational field. *Icarus* 88, 129-145 (1990).

- Ida, S., Makino, J. Scattering of planetesimals by a protoplanet - Slowing down of runaway growth. *Icarus* 106, 210 (1993)

- Ida, S., Guillot, T., Morbidelli, A. Accretion and destruction of planetesimals in turbulent disks.*Astroph. J.*, 686, 1292-1301.

- Kenyon, S. J., Luu, J. X. Accretion in the Early Kuiper Belt. I. Coagulation and Velocity Evolution. *Astronomical Journal* 115, 2136-2160 (1998).

- Kenyon, S. J., Luu, J. X. Accretion in the Early Outer Solar System. *Astrophysical Journal* 526, 465-470 (1999).

- Kenyon, S. J., Bromley, B. C. Gravitational Stirring in Planetary Debris Disks. *Astronomical Journal* 121, 538-551 (2001).

- Kokubo, E., Ida, S. Orbital evolution of protoplanets embedded in a swarm of planetesimals. *Icarus* 114, 247-257 (1995).

- Kokubo, E., Ida, S. On Runaway Growth of Planetesimals. *Icarus* 123, 180-191 (1996).

- Kokubo, E., Ida, S. Oligarchic Growth of Protoplanets. *Icarus* 131, 171-178 (1998).

- Laughlin, G., Steinacker, A., Adams, F. C. Type I Planetary Migration with MHD Turbulence. *Astrophysical Journal* 608, 489-496 (2004).

- Levison, H. F., Morbidelli, A. Models of the collisional damping scenario for ice-giant planets and Kuiper belt formation. *Icarus* 189, 196-212 (2007).

- Marzari, F., Davis, D., Vanzani, V. Collisional evolution of asteroid families. *Icarus* 113, 168-187 (1995).

- Nelson, R. P., Papaloizou, J. C. B. The interaction of giant planets with a disc with MHD turbulence - IV. Migration rates of embedded protoplanets. *Monthly Notices of the Royal Astronomical Society* 350, 849-864 (2004).

- Nelson, R. P. On the orbital evolution of low mass protoplanets in turbulent, magnetised disks. *Astronomy and Astrophysics* 443, 1067-1085 (2005)

- Ohtsuki, K., Stewart, G. R., Ida, S. Evolution of Planetesimal Velocities Based on Three-Body Orbital Integrations and Growth of Protoplanets. *Icarus* 155, 436-453 (2002).

- Ohtsuki, K. Rotation rate and velocity dispersion of planetary ring particles with size distribution. *Icarus* 183, 373-383 (2006).

- Ohtsuki, K. Rotation rate and velocity dispersion of planetary ring particles with size distribution II. Numerical simulation for gravitating particles. *Icarus* 183, 384-395 (2006).

- Shampine, L. F., and Gordon, M. *Computer Solution of Ordinary Differential Equations : The Initial Value Problem* (1975).

- Stern, S. A. On the Collisional Environment, Accretion Time Scales, and Architecture of the Massive, Primordial Kuiper Belt. *Astronomical Journal* 112, 1203 (1996).

- Stewart, G. R., Ida, S. 2000. Velocity Evolution of Planetesimals: Unified Analytical Formulas and Comparisons with N-Body Simulations. *Icarus* 143, 28-44 (2000).

- Stewart, S. T., Leinhardt, Z. M. 2009. Velocity-Dependent Catastrophic Disruption Criteria for Planetesimals. Astrophysical Journal 691, L133-L137.

- Wetherill, G. W. Collisions in the asteroid belt. *Journal of Geophysical Research* 72, 2429-2444 (1967).

- Wetherill, G. W. Comparison of analytical and physical modeling of planetesimal accumulation. *Icarus* 88, 336-354 (1990).

- Wetherill, G. W., Stewart, G. R. Formation of planetary embryos - Effects of fragmentation, low relative velocity, and independent variation of eccentricity and inclination. *Icarus* 106, 190 (1993).

- Wetherill, G. W., Stewart, G. R. Accumulation of a swarm of small planetesimals. *Icarus* 77, 330-357 (1989).